JPE 16-3-19

http://dx.doi.org/10.6113/JPE.2016.16.3.1012
ISSN(Print): 1598-2092 / ISSN(Online): 2093-4718

Sensor Fault Detection, Localization, and System Reconfiguration with a Sliding Mode Observer and Adaptive Threshold of PMSM

Aibeche Abderrezak[†] and Kidouche Madjid[*]

[†,*]Dept. of Automation, Applied Automation Laboratory, University of Boumerdes, Boumerdes, Algeria

Abstract

This study deals with an on-line software fault detection, localization, and system reconfiguration method for electrical system drives composed of three-phase AC/DC/AC converters and three-phase permanent magnet synchronous machine (PMSM) drives. Current sensor failure (outage), speed/position sensor loss (disconnection), and damaged DC-link voltage sensor are considered faults. The occurrence of these faults in PMSM drive systems degrades system performance and affects the safety, maintenance, and service continuity of the electrical system drives. The proposed method is based on the monitoring signals of "abc" currents, DC-link voltage, and rotor speed/position using a measurement chain. The listed signals are analyzed and evaluated with the generated residuals and threshold values obtained from a Sliding Mode Current-Speed-DC-link Voltage Observer (SMCSVO) to acquire an on-line fault decision. The novelty of the method is the faults diagnosis algorithm that combines the use of SMCSVO and adaptive thresholds; thus, the number of false alarms is reduced, and the reliability and robustness of the fault detection system are guaranteed. Furthermore, the proposed algorithm's performance is experimentally analyzed and tested in real time using a dSPACE DS 1104 digital signal processor board.

Key words: Adaptive threshold, Fault diagnosis, Permanent magnet synchronous machines, Sliding mode

I. INTRODUCTION

The recent significant improvement in the reliability of variable speed drive systems is attributed to the technological development in power electronics, digital signal processors (DSPs), computer science, and electrical engineering. The specified requirements, such as protection, safety, and continuity of service, mainly protect users and electrical systems from electrical drive system faults [1]–[3].

Permanent magnet synchronous machine (PMSM) drives have the advantages of high efficiency, high power density with low weight, and easy high-speed operation. PMSM drives are utilized in electrical drive systems that have become highly interesting in the past years. Owing to their advantages, PMSM drives are increasingly used in electric traction "vehicles, tramways, high-speed trains…", aerospace, aeronautics, nuclear power plants, wind energy conversion systems, and many industrial applications of variable speed drives [2]–[7].

The PMSM drive system is a combination of electrical, electronic, and mechanical components. It is composed of a power source, a rectifier, a DC-link bus (filter), an inverter voltage-source converter (VSC), PMSM motor drives, and a control component. The control system should be based on the measured information in the motor and power electronics in real time. Otherwise, these components would present many faults [6], [8]–[12].

Different fault-tolerant operation methods that involve reconfiguring topologies and control strategies are adopted to improve the reliability of electrical systems [3], [6], [8]–[14].

Sliding-mode observer (SMO) is one of the most attractive methods that can accurately estimate the state of PMSM drives [1], [2], [15], [16]. A disadvantage of this method is that an undesirable chattering phenomenon is inevitable in the estimated variables. To solve this problem, a robust method was proposed in [16] to avoid the use of a low-pass filter, and the position compensation, sign-num, and

Manuscript received Sep. 22, 2015; accepted Jan. 24, 2016
Recommended for publication by Associate Editor Kyo-Beum Lee.
[†]Corresponding Author: aibeche_umbb@univ-boumerdes.dz
Tel: +213-661-265492, University of Boumerdes
[*]Dept. of Automation, Applied Automation Laboratory, University of Boumerdes, Algeria

saturation functions are replaced with the sigmoid function.

The extended phase-locked loop (EPLL) algorithm described in [5] combined with SMO is adopted to estimate rotor speed and reconstruct the rotor position.

The reliability of PMSM/PWM-VSC drive systems depends on the reliability of power conversion systems (rectifiers and inverters) and measurement sensors [9], [17]–[19]. The reliability of power conversion systems was analyzed and investigated in [3], [4], [8], [9], [20], and [21]. Approximately 38% of the faults in the voltage-source power conversion systems were due to the failures of power devices, such as the insulated-gate bipolar transistor (IGBT) (short-circuit and open-switch faults) [8]. A fault in the sensors (current, speed, and DC-link voltage) can cause instability in the control loops of the system [11], [12], [18], [19]. The data measured by current, DC-link voltage, and speed/position sensors are extremely important in determining the reliability, the control system performances, and the efficiency of PMSM drive systems [10]–[14], [17]–[19].

Accurate and robust algorithm for detection, localization, and reconfiguration sensors faults are required to guarantee safety, maintenance, and service continuity. The problems of these sensors are described and detailed in many researches [10]–[14], [17]–[19]. In these studies, the majority of diagnostic methods for existing sensor faults are based on a fixed threshold. However, threshold values depend on operating conditions (speed, load). This condition exerts a negative effect on the performance of these methods and leads to the generation of false alarms. Accordingly, the method proposed in this study is based on monitoring the evolution of thresholds and residues values of the measured data according to the speed and load of the system. The proposed method fully considers the independence of the system residuals.

We consider that faults occur in the essential sensors of the control system. Then, the SMO is applied to estimate the stator currents, rotor speed/position, and DC-link voltage, and the adaptive threshold is utilized to reduce false alarms. The validity of the proposed algorithm is verified through a comprehensive set of experiments.

II. Mathematical Model of PMSM

Generally, mathematical models of electrical machine AC drives are based on several simplifying assumptions, such as those presented in [1], [6], [7], namely, stator windings are assumed to be perfectly sinusoidally distributed; the fundamental component is considered due to the sinusoidal distribution of magnetic fields; and magnetic saturation, hysteresis losses, and leakage flux are ignored. With these assumptions, the mathematical model of PMSM drives can be modeled by using a natural (*abc*) reference frame.

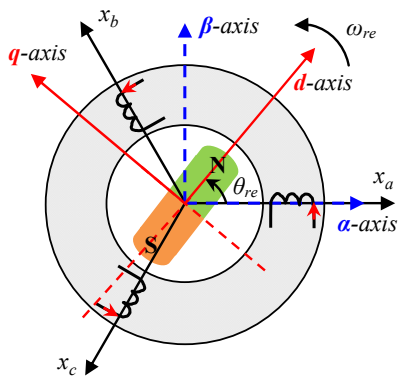

Fig. 1. Layout of PMSM drives in different reference frames.

$$\begin{cases} [v_{abc}(t)] = [R_s][i_{abc}(t)] + \dfrac{d}{dt}[\lambda_{abc}(t)] \\ [\lambda_{abc}(t)] = [L_s][i_{abc}(t)] + [\lambda_{m\_abc}(t)] \end{cases}, \tag{1}$$

where $[v_{abc}(t)]=[\ v_a(t)\ v_b(t)\ v_c(t)]^T$ and $[i_{abc}(t)]=[\ i_a(t)\ i_b(t)\ i_c(t)]^T$ are the stator phase voltage and current vectors, respectively; $[\lambda_{abc}(t)]=[\ \lambda_a(t)\ \lambda_b(t)\ \lambda_c(t)]^T$ is the stator flux linkage vector; $[R_s]=[R_{sa}\ \ R_{sb}\ \ R_{sc}]^T$; R_{sn} is the resistance of phase "n" ($R_{sa}=R_{sb}=R_{sc}=R_s$); $[L_s]$ is the inductance matrix that contains self and mutual inductances; $[\lambda_{m\_abc}(t)]$ is the flux through the stator windings matrix caused by the permanent magnet being defined as:

$$\left[\lambda_{m\_abc}(t)\right] = \left[\lambda_m.\sin(\theta_{re} - \theta_{o\_abc})\right], \tag{2}$$

where θ_{re} is the electrical rotor position, λ_m is the flux linkage generated by permanent magnets, and θ_{o_abc} is the initial electrical phase for a three-phase machine $\theta_{o\_abc}=0, -120°, -240°$.

The Concordia and Park transformations are usually utilized to express the variables in stationary and rotational reference frames to obtain the PMSM model in two axes.

The relationships among these reference frames are illustrated in Fig. 1 and expressed as:

$$\begin{bmatrix} x_{sd}^{(s)}(t) \\ x_{sq}^{(s)}(t) \end{bmatrix} = \sqrt{\frac{2}{3}} \begin{bmatrix} 1 & -\frac{1}{2} & -\frac{1}{2} \\ 0 & \frac{\sqrt{3}}{2} & -\frac{\sqrt{3}}{2} \end{bmatrix} \begin{bmatrix} x_a(t) \\ x_b(t) \\ x_c(t) \end{bmatrix}, \tag{3}$$

$$\begin{bmatrix} x_{sd}^{(r)}(t) \\ x_{sq}^{(r)}(t) \end{bmatrix} = \begin{bmatrix} \cos(\theta_{re}) & \sin(\theta_{re}) \\ -\sin(\theta_{re}) & \cos(\theta_{re}) \end{bmatrix} \begin{bmatrix} x_{sd}^{(s)}(t) \\ x_{sq}^{(s)}(t) \end{bmatrix}, \tag{4}$$

where $x(t)$ represents the voltage, current, or flux variables and θ_{re} is the electrical position of the rotor.

These transformations simplify the dynamic equations of the machine that facilitates their study and analysis (control, diagnosis, detection, localization, and reconfiguration faults). By applying transformations (3) and (4) to system (1), the dynamic models of PMSM drives in the $(d\text{-}q)$ rotational and $(\alpha\text{-}\beta)$ stationary reference frames are represented in Equs. (5) and (6), respectively.

$$\begin{cases} \dfrac{di_{sd}^{(r)}}{dt} = \dfrac{1}{L_d} v_{sd}^{(r)} - \dfrac{R_s}{L_d} i_{sd}^{(r)} + \dfrac{L_q}{L_d} i_{sq}^{(r)} P\omega_m \\ \dfrac{di_{sq}^{(r)}}{dt} = \dfrac{1}{L_q} v_{sq}^{(r)} - \dfrac{R_s}{L_q} i_{sq}^{(r)} - \dfrac{L_d}{L_q} i_{sd}^{(r)} P\omega_m - \dfrac{\lambda_m}{L_q} P\omega_m \\ \dfrac{d\omega_m}{dt} = \dfrac{1}{J}\left[T_e - B\omega_m(t) - T_L\right] \\ T_e = \dfrac{3}{2} P\left[\lambda_m i_{sq}^{(r)} + \Delta L_{dq} i_{sd}^{(r)} i_{sq}^{(r)}\right] \end{cases}, \quad (5)$$

where $v_{sd}^{(r)}$, $v_{sq}^{(r)}$, $i_{sd}^{(r)}$, $i_{sq}^{(r)}$, R_s, L_d, L_q, θ_m, ω_m, ω_{re}, B, J, T_L, P, and ΔL_{dq} are the stator voltages and currents in the *(d-q)* reference frame, resistance, *d-* and *q-axis* inductances, mechanical rotor position, rotor speed, electrical angular rotor speed (ω_{re} =P. ω_m =$P.d\theta_m/dt$), viscous friction coefficient, inertia, load torque, number of pole pairs, respectively, and ΔL_{dq} =L_d-L_q . ΔL_{dq} is nonzero for a salient-pole PMSM, whereas ΔL_{dq} is zero for a nonsalient-pole PMSM.

$$\begin{cases} \dfrac{di_{sd}^{(s)}}{dt} = \dfrac{1}{L_d} v_{sd}^{(s)} - \dfrac{R_s}{L_d} i_{sd}^{(s)} - \dfrac{\Delta L_{dq}}{L_d} i_{sq}^{(s)} P\omega_m + \dfrac{\eta}{L_d}\sin\theta_{re} \\ \dfrac{di_{sq}^{(s)}}{dt} = \dfrac{1}{L_d} v_{sq}^{(s)} - \dfrac{R_s}{L_d} i_{sq}^{(s)} + \dfrac{\Delta L_{dq}}{L_d} i_{sd}^{(s)} P\omega_m - \dfrac{\eta}{L_d}\cos\theta_{re} \\ T_e = \dfrac{3}{2} P \begin{bmatrix} \lambda_m[i_{sq}^{(s)}\cos\theta_{re} - i_{sd}^{(s)}\sin\theta_{re}] + [i_{sd}^{(s)} i_{sq}^{(s)}\cos 2\theta_{re} \\ + [(i_{sq}^{(s)})^2 - (i_{sd}^{(s)2})]\cos\theta_{re}\sin\theta_{re}]\Delta L_{dq} \end{bmatrix} \end{cases}, \quad (6)$$

where $\eta = \Delta L_{dq}.(\omega_{re} i_{sd}^{(r)} - Si_{sq}^{(r)}) + \lambda_m.\omega_{re}$ is the magnitude of the extended back electromotive force (EMF) term; $v_{sd}^{(s)}$, $v_{sq}^{(s)}$, $i_{sd}^{(s)}$, $i_{sq}^{(s)}$ are the stator voltages and currents in the (α-β) reference frame, respectively; and S is the derivative operator.

III. Proposed Fault Diagnosis Method

A. Design of a Sliding-mode Current–Speed–DC-link Voltage Observer (SMCSVO)

The information on PMSM stator currents, rotor speed/position, and DC-link voltage is essential to the control system PWM-SVM. In this study, "SMCSVO" is designed to estimate this information [15], [16].

With Eqn. (6), SMCSVO can be designed as:

$$\begin{cases} \dfrac{d}{dt}\hat{i}_{sdq}^{(s)} = \dfrac{1}{L_d} v_{sdq}^{(s*)} - \dfrac{R_s}{L_d}\hat{i}_{sdq}^{(s)} + \omega_{re}\dfrac{\Delta L_{dq}}{L_d}\begin{bmatrix} 0 & -1 \\ 1 & 0 \end{bmatrix} i_{sdq}^{(s)} - \\ \dfrac{1}{L_d} K_{SMO} H(\tilde{i}_{sdq}^{(s)}) \\ \dfrac{d}{dt}\hat{\lambda}_{sdq}^{(s)}(t) = v_{sdq}^{(s*)} - R_s\hat{i}_{sdq}^{(s)} + K_\lambda H(\tilde{i}_{sdq}^{(s)}) \end{cases}, \quad (7)$$

where K_{SMO}, K_λ are the positive gain constants of the current and flux observers, respectively; $\hat{i}_{sdq}^{(s)}$ and $\hat{\lambda}_{sdq}^{(s)}$ are the estimated stator current and flux vectors, respectively; $v_{sdq}^{(s*)}$ is the reconstructed stator voltage vector; $\tilde{i}_{sd}^{(s)} = i_{sd}^{(s)} - \hat{i}_{sd}^{(s)}$ and $\tilde{i}_{sq}^{(s)} = i_{sq}^{(s)} - \hat{i}_{sq}^{(s)}$ are the current errors between measured and estimated stator currents; $H(\tilde{i}_{sd}^{(s)})$, $H(\tilde{i}_{sq}^{(s)})$ are the sigmoid functions based on the error of the estimated and actual stator currents, respectively. The values of these functions are: $(-1 < H(\tilde{i}_{sdq}^{(s)}) < 1)$.

Many variations of Eqn. (8) can be found in literature, e.g., using the signum function or the saturation function [1], [2], [15], [16]. In this work, the sigmoid function is selected to replace the signum function to reduce the undesirable chattering problem [16].

The property of the sigmoid function can be expressed as:

$$\left[H\left(\tilde{i}_{sdq}^{(s)}(t)\right)\right] = \left[\left(\frac{2}{1+\exp(-a(t).\tilde{i}_{sdq}^{(s)}(t))}\right) - 1\right], \quad (8)$$

where "a" is a positive coefficient used to regulate the slope of the sigmoid function.

The PMSM phase voltage $v_{sa}^{(s)}$,$v_{sb}^{(s)}$ and $v_{sc}^{(s)}$ can be reconstituted using the measured DC-bus voltage V_{dc_m} and the inverter switching states (S_a,S_b,S_c) as follows:

$$\begin{bmatrix} v_{sa}^{(*)} \\ v_{sb}^{(*)} \\ v_{sc}^{(*)} \end{bmatrix} = \frac{V_{dc\_m}}{3}.\begin{bmatrix} 2 & -1 & -1 \\ -1 & 2 & -1 \\ -1 & -1 & 2 \end{bmatrix}\begin{bmatrix} S_a \\ S_b \\ S_c \end{bmatrix}, \quad (9)$$

In the stationary (α-β) frame, the previous stator voltages can be written as:

$$\begin{aligned} \begin{bmatrix} v_{sd}^{(s*)} \\ v_{sq}^{(s*)} \end{bmatrix} &= \sqrt{\frac{2}{3}}\begin{bmatrix} 1 & -\frac{1}{2} & -\frac{1}{2} \\ 0 & \frac{\sqrt{3}}{2} & -\frac{\sqrt{3}}{2} \end{bmatrix}.\begin{bmatrix} v_{sa}^{(*)} \\ v_{sb}^{(*)} \\ v_{sc}^{(*)} \end{bmatrix} \\ &= V_{dc\_m}.\begin{bmatrix} \frac{2}{\sqrt{6}} & -\frac{1}{\sqrt{6}} & -\frac{1}{\sqrt{6}} \\ 0 & \frac{1}{\sqrt{2}} & -\frac{1}{\sqrt{2}} \end{bmatrix}.\begin{bmatrix} S_a \\ S_b \\ S_c \end{bmatrix} \end{aligned}, \quad (10)$$

where $[v_{sdq}^{(s*)}]$ is the input voltage to SMCSVO.

The relationship between the switching states (S_a,S_b,S_c) and voltage vector $[v_{sdq}^{(s*)}]$ can be expressed as:

$$\begin{bmatrix} v_{sd}^{(s*)} \\ v_{sq}^{(s*)} \end{bmatrix} = V_{dc\_m}.\begin{bmatrix} x \\ y \end{bmatrix} = V_{dc\_m}.\begin{bmatrix} 1/\sqrt{6}(2S_a - S_b - S_c) \\ 1/\sqrt{2}(S_b - S_c) \end{bmatrix}, \quad (11)$$

From Eqn. (11), the *α-axis* and *β-axis* voltages can be obtained for various states by varying the switching vector, $[S_a\ S_b\ S_c]^T$.

The DC-link voltage is sensitive to speed variations (speed reversal operations and speed change) and load changes (sudden). In fact, a variation of the DC-link voltage causes the

output of the control loop to change and the PWM signals to vary to maintain the desired speed or torque. This phenomenon can affect the perfect management of the electrical power and its transfers of the rectifier-inverter and machine [3], [10]–[13], [19]. Software redundancy (virtual sensor) should be set up in our system to monitor the DC-link voltage sensor to avoid the undesirable consequences of the DC-link voltage faults on performance or possibly on the safety of the operating electrical system. As result, the DC-link voltage is estimated using the rated voltage (constant) and duty cycles.

The dynamics of the DC link voltage can be defined as:

$$V_{dc\_m} = \mu . V_{dc\_n}, \tag{12}$$

where μ is a gain determined based on the PWM-switching approach.

If the DC-link voltage is not measured, it is estimated by:

$$\hat{V}_{dc} = \hat{\mu} . V_{dc\_n}, \tag{13}$$

where V_{dc_n} and $\hat{V}_{dc}$ are the nominal and observed DC-link voltages, respectively.

The real DC-link voltage is determined by accurately estimating μ. Thus, the dynamic estimation error of the DC-link voltage is defined by:

$$\tilde{V}_{dc} = (\mu - \hat{\mu}) V_{dc\_n} = \tilde{\mu} . V_{dc\_n}, \tag{14}$$

By substituting the terms with Equs. (12) and (13) in Equ. (11), the stator voltage vector $[v_{sdq}^{(s^*)}]$ is expressed as:

$$\begin{bmatrix} v_{sd}^{(s^*)} \\ v_{sq}^{(s^*)} \end{bmatrix} = V_{dc\_m} \cdot \begin{bmatrix} x \\ y \end{bmatrix} = \mu . V_{dc\_n} \cdot \begin{bmatrix} x \\ y \end{bmatrix}, \tag{15}$$

From Eqn. (15), the stator voltages are reconstructed using the nominal DC-bus V_{dc_n}, the estimate coefficient $\hat{\mu}$, and the states of the power switches as follows:

$$\begin{bmatrix} \hat{v}_{sd}^{(s^*)} \\ \hat{v}_{sq}^{(s^*)} \end{bmatrix} = \hat{V}_{dc} \cdot \begin{bmatrix} x \\ y \end{bmatrix} = \hat{\mu} . V_{dc\_n} \cdot \begin{bmatrix} x \\ y \end{bmatrix}, \tag{16}$$

where $\hat{v}_{sd}^{(s^*)}$ and $\hat{v}_{sq}^{(s^*)}$ are the estimated stator voltages and the new inputs of SMCSVO, respectively.

From Equs. (7), (13), and (16), the design of a sliding mode for the current, flux, and DC-link voltage observers is synthesized as follows:

$$\begin{cases} \frac{d}{dt}\hat{i}_{sdq}^{(s)} = \frac{1}{L_d}\hat{v}_{sdq}^{(s^*)} - \frac{R_s}{L_d}\hat{i}_{sdq}^{(s)} + \omega_{re}\frac{\Delta L_{dq}}{L_d}\begin{bmatrix} 0 & -1 \\ 1 & 0 \end{bmatrix} i_{sdq}^{(s)} - \\ \frac{1}{L_d} K_{SMO} H\left(\tilde{i}_{sdq}^{(s)}\right) \\ \frac{d}{dt}\hat{\lambda}_{sdq}^{(s)} = \hat{v}_{sdq}^{(s^*)} - R_s \hat{i}_{sdq}^{(s)} + K_\lambda H(\tilde{i}_{sdq}^{(s)}) \\ \hat{V}_{dc} = \hat{\mu} . V_{dc\_n} \end{cases}, \tag{17}$$

From Equs. (7), (14), and (17), the estimation error dynamics for stator currents, flux, and DC-link voltage are obtained as follows:

$$\begin{cases} \frac{d}{dt}\tilde{i}_{sdq}^{(s)} = -\frac{R_s}{L_d}\tilde{i}_{sdq}^{(s)} + \tilde{\mu} . V_{dc\_nom} \cdot \frac{1}{L_d}\begin{bmatrix} x \\ y \end{bmatrix} + \\ \frac{1}{L_d} K_{SMO} H(\tilde{i}_{sdq}^{(s)}) - \frac{1}{L_d}\begin{bmatrix} 1 & 0 \\ 0 & 1 \end{bmatrix} e_{sdq}^{(s)} \\ \frac{d}{dt}\tilde{\lambda}_{sdq}^{(s)} = -R_s \tilde{i}_{sdq}^{(s)} + \tilde{\mu} . V_{dc\_nom} \cdot \begin{bmatrix} x \\ y \end{bmatrix} - K_\lambda H(\tilde{i}_{sdq}^{(s)}) \end{cases}, \tag{18}$$

$$\begin{bmatrix} e_{sd}^{(s)} \\ e_{sq}^{(s)} \end{bmatrix} = \eta . \begin{bmatrix} -\sin(\theta_{re}) \\ \cos(\theta_{re}) \end{bmatrix}, \tag{19}$$

where $e_{sd}^{(s)}$ and $e_{sq}^{(s)}$ are the back-EMF voltage components. Sliding surface S_n can be defined as:

$$S_n = [\tilde{i}_{sd}^{(s)} \ \tilde{i}_{sq}^{(s)} \ \tilde{\lambda}_{sd}^{(s)} \ \tilde{\lambda}_{sq}^{(s)} \ \tilde{\mu}] = [0 \quad 0 \quad 0 \quad 0 \quad 0], \tag{20}$$

By accurately selecting K_{SMO}, K_λ, and $\hat{\mu}$, we can guarantee the candidate Lyapunov function $V = S_n^T . S_n / 2 > 0$ and d$V/dt<0$, so asas well as observer stability. The following Lyapunov function is considered to analyze stability.

$$V = \frac{1}{2}\left((\tilde{i}_{sd}^{(s)})^2 + (\tilde{i}_{sq}^{(s)})^2 + (\tilde{\lambda}_{sd}^{(s)})^2 + (\tilde{\lambda}_{sq}^{(s)})^2 + \frac{\tilde{\mu}^2}{K_\mu} \right) > 0, \tag{21}$$

The time derivative of the Lyapunov function is established as:

$$\dot{V} = \tilde{i}_{sd}^{(s)} \frac{d\tilde{i}_{sd}^{(s)}}{dt} + \tilde{i}_{sq}^{(s)} \frac{d\tilde{i}_{sq}^{(s)}}{dt} + \tilde{\lambda}_{sd}^{(s)} \frac{d\tilde{\lambda}_{sd}^{(s)}}{dt} + \tilde{\lambda}_{sq}^{(s)} \frac{d\tilde{\lambda}_{sq}^{(s)}}{dt} + \frac{\tilde{\mu}}{K_\mu}\frac{d\tilde{\mu}}{dt}, \tag{22}$$

where K_μ is a positive updating gain of the DC-link voltage observer. By substituting the current and flux derivation terms with Equ. (17), Equ. (22) is derived.

$$\begin{aligned} \dot{V} = & -\frac{R_s}{L_d}\left[(\tilde{i}_{sd}^{(s)})^2 + (\tilde{i}_{sq}^{(s)})^2 \right] + \\ & \frac{1}{L_d}\left[K_{SMO}\left(\tilde{i}_{sd}^{(s)} H(\tilde{i}_{sd}^{(s)}) + \tilde{i}_{sq}^{(s)} H(\tilde{i}_{sq}^{(s)}) \right) - \left(\tilde{i}_{sd}^{(s)} e_{sd}^{(s)} + \tilde{i}_{sq}^{(s)} e_{sq}^{(s)} \right) \right] - \\ & \left[K_\lambda \left(\tilde{\lambda}_{sd}^{(s)} H(\tilde{i}_{sd}^{(s)}) + \tilde{\lambda}_{sq}^{(s)} H(\tilde{i}_{sq}^{(s)}) \right) + R_s \left(\tilde{i}_{sd}^{(s)} \tilde{\lambda}_{sd}^{(s)} + \tilde{i}_{sq}^{(s)} \tilde{\lambda}_{sq}^{(s)} \right) \right] + \\ & \tilde{\mu}\left[V_{dc\_nom}\left(\frac{1}{L_d} x \tilde{i}_{sd}^{(s)} + \frac{1}{L_d} y \tilde{i}_{sq}^{(s)} + x \tilde{\lambda}_{sd}^{(s)} + y \tilde{\lambda}_{sq}^{(s)} \right) - \frac{\dot{\hat{\mu}}}{K_\mu} \right] \end{aligned}, \tag{23}$$

To ensure the negativity of Equ. (23), the adaptive gains can be designed by:

$$\begin{cases} \dot{\hat{\mu}} = K_\mu . V_{dc\_nom} \cdot \left[\frac{1}{L_d} x \tilde{i}_{sd}^{(s)} + \frac{1}{L_d} y \tilde{i}_{sq}^{(s)} + x \tilde{\lambda}_{sd}^{(s)} + y \tilde{\lambda}_{sq}^{(s)} \right] \\ K_{SMO} = \frac{[\tilde{i}_{sd}^{(s)} e_{sd}^{(s)} + \tilde{i}_{sq}^{(s)} e_{sq}^{(s)}]}{[\tilde{i}_{sd}^{(s)} H(\tilde{i}_{sd}^{(s)}) + \tilde{i}_{sq}^{(s)} H(\tilde{i}_{sq}^{(s)})]} \\ K_\lambda = \frac{-R_s [\tilde{i}_{sd}^{(s)} \tilde{\lambda}_{sd}^{(s)} + \tilde{i}_{sq}^{(s)} \tilde{\lambda}_{sq}^{(s)}]}{[\tilde{\lambda}_{sd}^{(s)} H(\tilde{i}_{sd}^{(s)}) + \tilde{\lambda}_{sq}^{(s)} H(\tilde{i}_{sq}^{(s)})]} \end{cases}, \tag{24}$$

If the sliding mode is enforced, the back EMF voltage components can be estimated in the following form:

$$\begin{cases} \hat{e}_{sd}^{(s)} = -\lambda_m \hat{\omega}_{re} \sin(\hat{\theta}_{re}) \cong K_{SMO} H(\tilde{i}_{sd}^{(s)}) \\ \hat{e}_{sq}^{(s)} = \lambda_m \hat{\omega}_{re} \cos(\hat{\theta}_{re}) \cong K_{SMO} H(\tilde{i}_{sq}^{(s)}) \end{cases}, \tag{25}$$

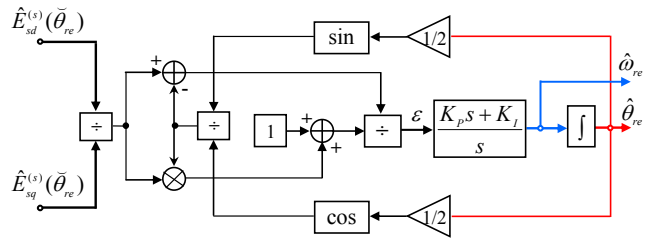

Fig. 2. Extended PLL block scheme.

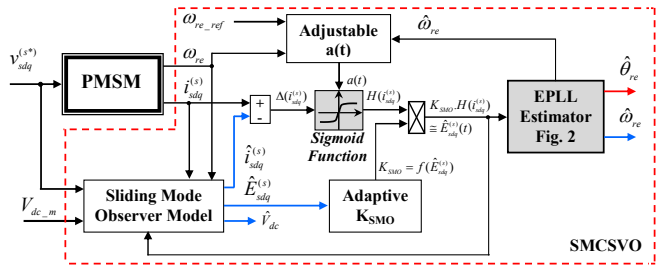

Fig. 3. Structure of the proposed observer.

The estimated rotor position can then be extracted from the estimated back-EMF voltage components as follows:

$$\hat{\theta}_{re} = \arctan 2[-\hat{e}_{sd}^{(s)}, \hat{e}_{sq}^{(s)}] \cong \arctan 2[-H(\tilde{i}_{sd}^{(s)}), H(\tilde{i}_{sq}^{(s)})] \quad (26)$$

The block scheme of this algorithm is shown in Fig. 2, and the proposed SMCSVO combined with the EPLL structure is illustrated in Fig. 3.

By using the EPLL algorithm, the rotor speed is observed from:

$$\hat{\omega}_{re} = \left(K_P + \frac{K_I}{S}\right).\varepsilon(t) = \left(K_P + \frac{K_I}{S}\right).tg\left(\bar{\theta}_{re} - \frac{\hat{\theta}_{re}}{2}\right), \quad (27)$$

where $\hat{\theta}_{re}$ is the argument of the feedback signals and represents the estimated rotor position, $\bar{\theta}_{re}$ represents the argument of the input waveforms, and (K_P, K_I) are the proportional and integral gains of the *PI* controller, respectively.

B. Proposed Fault Diagnosis Method

1) Hardware and Software System Configuration

The hardware and software system configuration for sensors fault diagnosis for the PMSM drive system using SMCSVO is shown in Fig. 4, including the control system, software supervision, a protection system, a PMSM, a voltage-source inverter (VSI), an AC source, and a data acquisition system based on the available measurements (phase currents, DC-link voltage, and mechanical rotor speed/position).

To perform the proposed configuration, the following steps are necessary:

- Sensing and processing of currents, rotor speed/position, and DC-link voltage.
- Accurate measurements of currents, rotor speed/position, and DC-link voltage.

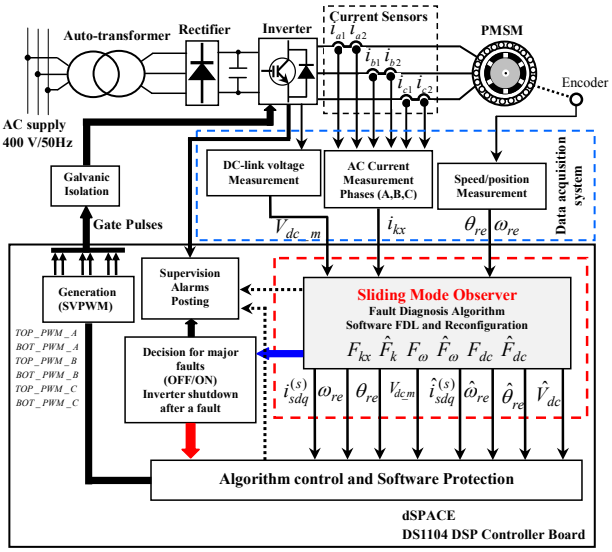

Fig. 4. Hardware and software system configuration.

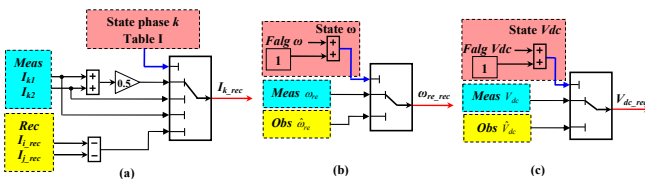

Fig. 5. (a) Logic circuit for current sensors FTLR. (b) Logic circuit for speed sensor FTLR. (c) Logic circuit for Vdc sensor FTLR.

- Measurement of the stator phase currents of the PMSM using Hall-effect current transducers; the fault diagnosis method is based on hardware redundancy with additional current sensors (two on each phase) and estimated current using a software algorithm (see Fig. 5(a)). The advantage of this technical method is increased, and reliability is guaranteed.
- Measurement of the rotor speed/position (ω_{re} or θ_{re}) using a rotor position encoder.
- Ensuring the accuracy of currents, rotor speed/position, and DC-link voltage observers.
- Performing the space vector PWM (SVPWM) by generating the gate signals for the VSI.
- Implementing the fault diagnosis algorithm by generating the significant coefficients, namely, $F_{kx}, \hat{F}_k, F_{dc}, \hat{F}_{dc}, F_\omega$, and $\hat{F}_\omega$.
- Ensuring the efficiency of software protection to inhibit the drive system in case of DC-link over-voltage/under-voltage, over-current, over-speed, ground fault, and major faults. These functions are performed by a hardware and software configuration.

2) Sensor Fault Detection, Localization, and Reconfiguration (FDLR)

a) Current Sensor FDLR Unit

The proposed FDLR algorithm of the current sensor is based on the sliding-mode current observer (SMCO) model and the current coefficients calculation. Two coefficients are calculated,

namely, one from measured current F_{kx} and the other through observed current $\hat{F}_{kx}$. The values of F_{kx} and $\hat{F}_{kx}$ are utilized in the FDLR method. They are defined as follows:

$$\begin{cases} F_{kx} = \dfrac{RMS(|I_{kx}|)}{Mean(|I_{kx}|)+\varepsilon} \\ \hat{F}_k = \dfrac{RMS(|\hat{I}_k|)}{Mean(|\hat{I}_k|)+\varepsilon} \end{cases}, \quad (28)$$

where $k=a,b,c$ is the number of phases, $x=1, 2$ is the number of current sensors (two per phase), and ε is a very small positive constant used to avoid the singularity of terms F_{kx} and $\hat{F}_{kx}$. Under normal operating conditions, the coefficients values are approximately equal to $(\pi/2\sqrt{2}=1.111)$.

When current sensor fault "outage" occurs, the coefficients values have different behavior instantaneous evolutions and therefore become practical for diagnostic purposes. Comparison of the two coefficients allows the detection, localization, and reconfiguration of the faulty current sensor. The main idea of the proposed FDLR method is to use $\hat{F}_{kx}$ as the adaptive threshold for F_{kx}, and both coefficients are independent of the variations in current, speed, and load transients. Accordingly, the adaptive thresholds are calculated as follows:

$$S_k = \hat{F}_k + \xi_I, \quad (29)$$

where ξ_I is a positive gain used to guarantee robust diagnosis and good separation between F_{kx} and $\hat{F}_k$, i.e., $0<\xi_I<1$.

To diagnose the current sensor fault, the following residual variables are considered:

$$r_{kx} = S_k - F_{kx} + k_I \quad (30)$$

Six residues are generated for the current sensors. These values are compared with the threshold values to detect faults.

k_I is a positive gain, $0<k_I<1$.

The fault flags of the current sensors can be provided as:

$$Flag\ I_{kx} = \begin{cases} 0\ if\ r_{kx} < S_k\ Healthy\ operations \\ 1\ if\ r_{kx} > S_k\ Faulty\ operations \end{cases}, \quad (31)$$

The logic circuit presented in Fig. 5(a) can identify the faulty sensor for a phase current fault and the reconfiguration system for a current sensor fault. Table I shows the configuration structure for this diagnosis system.

b) Speed Sensor FDLR Unit

Before the occurrence of a speed sensor fault, the PMSM motor control system is based on a vector-controlled algorithm with speed sensor feedback. After a speed sensor fault is detected, the PMSM motor control system is based on a vector-controlled algorithm with speed sensorless feedback using the sliding mode speed observer (SMSO) model in Fig. 4.

Two coefficients are calculated, namely,

TABLE I
INCIDENCE TABLE WITH A SIX-SENSORS RECONFIGURATION

Sensors k_x	Faulty	Flags (I_{kx})		State ph(k)	Residuals	Phase (k)
$k1$ $k2$	No Fault	0	0	1	$r_{k1}> s_k$ *and* $r_{k2}> s_k$	$I_{k\_rec}= 0.5(I_{k1}+I_{k2})$
	$k1$	1	0	2	$r_{k1}< s_k$ *and* $r_{k2}> s_k$	$I_{k\_rec}=I_{k2}$
	$k2$	0	1	3	$r_{k1}> s_k$ *and* $r_{k2}< s_k$	$I_{k\_rec}=I_{k1}$
	$k1$ and $k2$	1	1	4	$r_{k1}< s_k$ *and* $r_{k2}< s_k$	$I_{k\_rec}= -I_{i\_rec}-I_{j\_rec}$
$x=(1, 2)$, $k=(a, b,)c$, $i=(a, b, c)$, $j=(a, b, c)$, *where* $i\neq k$, $i\neq j$ *and* $j\neq k$, 0: healthy operations, 1: faulty operations						

$$\begin{cases} F_\omega = \left|\dfrac{\omega_{re}-\hat{\omega}_{re}}{\omega_{re}+\omega_{nom}}\right| \\ \hat{F}_\omega = \left|\dfrac{\hat{\omega}_{re}}{\omega_{nom}}\right| \end{cases}, \quad (33)$$

Under normal operating conditions, the values of the two coefficients are different, that is, $F_\omega \approx 0$ and $0<\hat{F}_\omega<1$. When a speed sensor experiences faulty "outage" the coefficient values are equal ($F_\omega = \hat{F}_\omega$).

To diagnose the speed sensor fault, the following residual variable is defined:

$$r_\omega = S_\omega - F_\omega + \xi_\omega, \quad (34)$$

where $S_\omega = \hat{F}_k$ is the adaptive threshold and ξ_ω is the positive gain used to guarantee robust diagnosis and ensure short-time fault detection. The value of ξ_ω is set to $0<\xi_\omega<0.1$.

The scheme of the speed sensor fault detection and isolation (FDI) unit is provided by the following:

- If $r_\omega>S_\omega$, we define *Flag* ω=0 and $\omega_{re\_rec}= \omega_{re\_m}$: normal;
- If $r_\omega<S_\omega$, we define *Flag* ω=1 and $\omega_{re\_rec} = \hat{\omega}_{re}$: fault;

where $\omega_{re} = \omega_{re\_m}$ is the output of the speed sensor and $\hat{\omega}_{re}$ is the output of the speed observer (SMO). *Flag* ω is the speed sensor fault flag. *Flag* ω=1 means that a speed sensor fault is detected; if it is zero, normal conditions exist. The logic circuit presented in Fig. 5(b) can identify the faulty sensor for a speed fault and the reconfiguration system for speed sensor fault.

c) DC-link Voltage Sensor FDLR Unit

The proposed FDLR algorithm of DC-link voltage sensor is based on the sliding mode voltage observer (SMVO) model and the calculation of the DC-link voltage coefficients. Two coefficients are calculated, namely, one from measured DC-link voltage F_{dc} and the other is through observed DC-link voltage $\hat{F}_{dc}$. The values of F_{dc} and $\hat{F}_{dc}$ in the FDLR

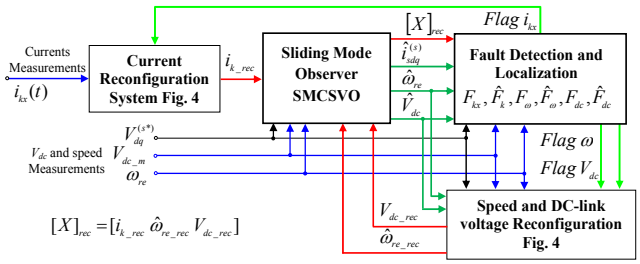

Fig. 6. Overall diagram for sensors FDLR.

method are defined as follows:

$$\begin{cases} F_{dc}=\left|\dfrac{V_{dc\_m}-\hat{V}_{dc}}{V_{dc\_m}+V_{dc\_n}}\right| \\ \hat{F}_{dc}=\left|\dfrac{\hat{V}_{dc}}{V_{dc\_n}}\right| \end{cases}, \tag{35}$$

The fault of the DC-link voltage sensor is detected by comparing the measured and observed DC-link voltages. In the case of normal operating conditions, the coefficients values $F_{dc}\to 0$ and $\hat{F}_{dc}\to 1$.

When the DC-link voltage sensor exhibits faulty "outage", the coefficients values are equal ($F_{dc}\approx\hat{F}_{dc}$).

To diagnose the DC-link voltage sensor fault, the following residual variable is defined:

$$r_{dc}=S_{dc}-F_{dc}+\xi_{dc}\,, \tag{36}$$

where $S_{dc}=\hat{F}_{dc}$ is the adaptive threshold and ξ_{dc} is the positive gain used to guarantee robust diagnosis to ensure short-time fault detection. The value of ξ_{dc} is set to $0<\xi_{dc}<0.5$. The scheme of the DC-link voltage sensor FDI unit is provided by the following:

- If $r_{dc}>S_{dc}$, we define *Flag* $V_{dc}=0$ and $V_{dc\_rec}=V_{dc\_m}$: normal;
- If $r_{dc}<S_{dc}$, we define *Flag* $V_{dc}=1$ and $V_{dc\_rec}=\hat{V}_{dc}$: fault.

where $V_{dc\_rec}=V_{dc\_app}$ is the input of the PWM-SVM controller and *Flag* V_{dc} is the DC-link voltage sensor fault flag. When a sensor fault is detected, the fault flag V_{dc} is set to 1; if it is zero, normal conditions exist. The logic circuit presented in Fig. 5(c) can identify the faulty sensor for a DC-link voltage fault and the reconfiguration system for a DC-link voltage sensor fault. A general scheme of the sensors FDLR of the proposed method is shown in Fig. 6.

IV. Experimental Results and Discussion

A. Experiment Stand Description

Practical testing of the proposed algorithm in real time is necessary. The principal objective of this implementation is to show in the behavior of the real electrical system in healthy and faulty or degraded operations in real time.

The architecture of the experimental system is shown in Fig. 7. The experimental platform is based on a 3 kW PMSM

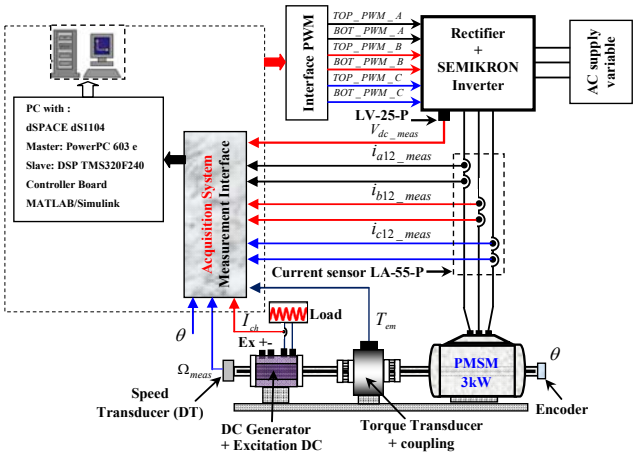

Fig. 7. Experimental setup of the 3 kW PMSM drive with a DS1104 controller.

supplied by a VSI controlled by PWM-SVM techniques. A dSPACE DS1104 controller board is utilized to validate and test the proposed algorithm in real time. The schematic of the experimental platform is presented in the Appendix.

The main components of the experimental system are described as follows.

- The PMSM is 3 kW, 360 V, 100 Hz, eight-pole, three-phases, and star-connected. The parameters of the PMSM are obtained from tests (DC tests, DC step test for identification L_d and L_q, back-EMF test, and speed decay test) in the Laboratory of Applied Automation (LAA/FHC/UMBB Algeria) and are reported in Appendix A.
- The PMSM is fed by a SEMIKRON inverter IGBT PWM-VSI, the data of which are reported in Appendix B.
- A DC generator with a variable resistor is utilized to load the PMSM to test the performance of the proposed algorithm with and without load.
- The stator phase currents and DC-link voltage are measured by Hall-type sensors LEM LA55-P and LV25-P, respectively.
- The position encoder 1024-pulse/rev is used for rotor position measurement, and the board's library is used to decode the position from the encoder digital signals.
- Microprocessor Control System: A dSPACE DS1104 control board is utilized to control the PMSM. This board consists of a power PC603e processor running at 250 MHz and Slave Texas Instruments' TMS320F240. The dSPACE real-time interface (RTI), Matlab real-time workshop (RTW), and the Simulink model are automatically converted into C-code, which is compiled and downloaded to the control board program memory. This conversion provides a fast and easy means to implement and test the control schemes in real time. RTI consists of a set of input/output interface blocks that connects the Simulink model to the real world [1], [6], [9], [17].

Experimental controls are performed with ControlDesk (ver 3.7.2), which is utilized to monitor different signals (currents, voltages, speed/position, and duty cycles) and tune the

parameters. ControlDesk is also interfaced with Simulink (MATLAB R2010a) and performs the necessary experiment tasks using a graphical interface.

B. Experimental Results

Prior to each operation, the DC offsets of currents, speed, and DC-link voltage are measured and must be eliminated. The measured noises of such signals are filtered with a first-order low-pass filter. The results presented in this section have three main goals, namely, to demonstrate the performance of SMCSVO with and without sensors faults, to show diagnostic immunity to false alarms resulting from transients (speed, currents, and loads), and to explain the capability to diagnose sensors faults.

The performances of the proposed method are tested as follows: speed reversal and profile change operations with healthy sensors (Fig. 8), evaluation of FDLR unit with current sensor fault (Fig. 9), evaluation of FDLR unit with speed sensor fault (Fig. 10), and evaluation of FDLR unit with DC-link voltage sensor fault (Fig. 11).

Fig. 8 shows the experimental results of estimated rotor speed/position, stator currents, and DC-link voltage, including stator fluxes and back EMF voltages using SMO. In this test, the performance of the proposed diagnostic method is verified during speed reversal operation [*450rpm to -450rpm,* T_L*=15%* T_n*,* V_{dc_n}*=507.6V,* $\varepsilon=10^{-5}$*,* $\xi_I=k_I=0.01$*,* $\xi_\omega=0.04$*,* $\xi_{dc}=0.05$] with healthy sensors.

The values of the dynamic coefficients μ and $\hat{\mu}$ of DC-link voltage are practically equal (Fig. 8(h)). The significant values of the residuals and thresholds generated are presented in Figs. 8(i), 8(j), and 8(k). The instantaneous values evolution of speed residual and threshold tracks the speed profile with healthy sensors. The speed residual r_ω value always remains above the corresponding threshold S_ω. The instantaneous values evolution of current residuals r_{kx} always remains below the corresponding thresholds S_k. The instantaneous value evolution of DC-link voltage residual r_{dc} always reamins below the corresponding threshold S_{dc}.

Figs. 8(i), 8(j), and 8(k) indicate that no false alarms are generated (all flags remain zero; see Fig. 8(l)), which demonstrates that the proposed FDLR method resists speed and load variations without generating any false alarms.

To ensure the verification of the proposed method SMCSVO, an important test with faulty sensors is presented in Figs. 9 to 11.

The experimental results presented in Fig. 9 illustrate the diagnostic method's capability to diagnose current sensors fault in the measurement chain. The operating conditions are as follows: ω_{re}*=450rpm,* T_L*=15% Tn,* V_{dc_n}*=507.6V*. The parameters of the FDLR algorithm are selected as follows: ε*=0.000055,* $\xi_I=k_I=0.5$*,* $\xi_\omega=0.04$*,* $\xi_{dc}=0.5$.

The FDLR algorithm for current sensor faults is presented in Section III.B.2.1. The scheme is based on hardware

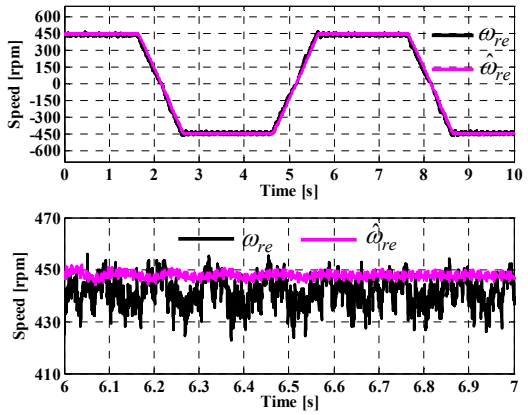

(a) Measured, observed, and reference rotor speed and their zooms.

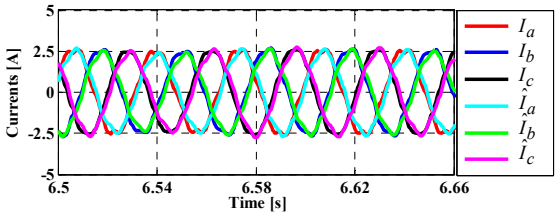

(b) Measured and observed stator currents.

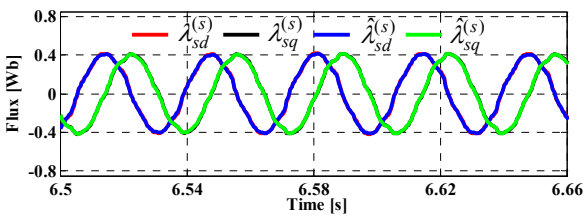

(c) Observed stator fluxes using the stator current model and SMO.

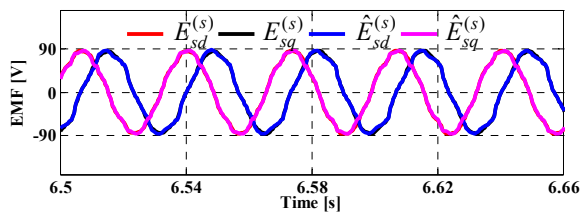

(d) Calculated and observed back EMF.

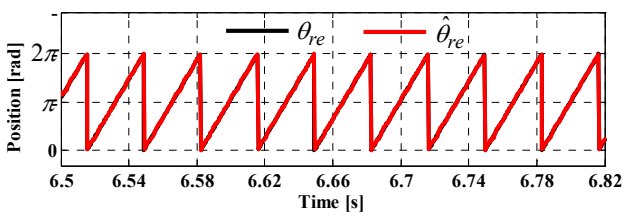

(e) Measured and observed rotor position.

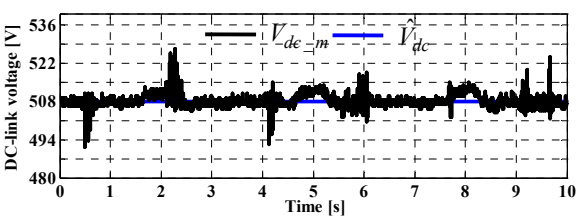

(f) Measured and observed DC-link voltage.

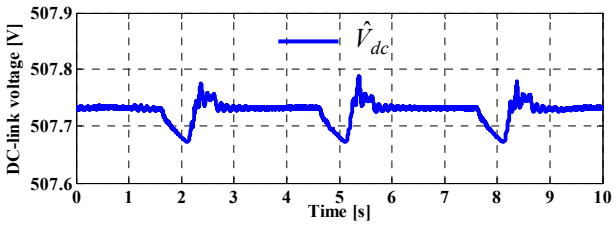

(g) Zoom: Observed DC-link voltage using SMO.

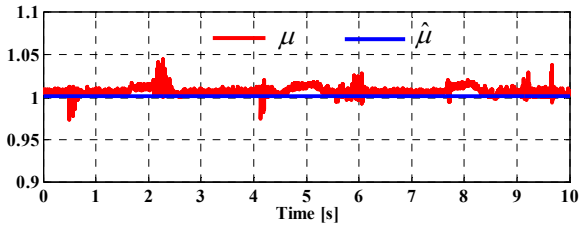

(h) Dynamic coefficients of DC-link voltage μ and $\hat{\mu}$.

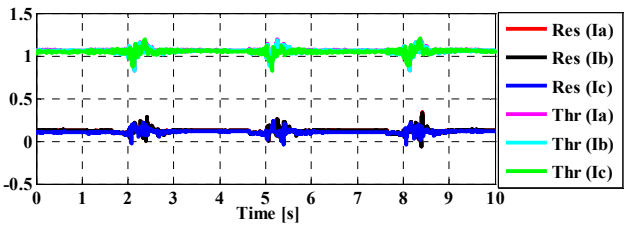

(i) Residual generation and thresholds of current sensors fault.

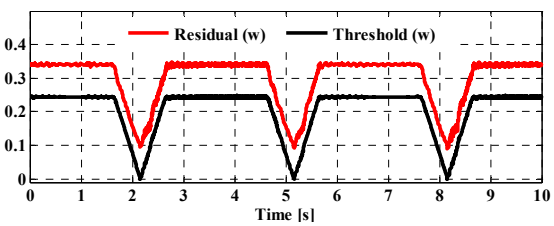

(j) Residual generation and threshold of speed sensor fault.

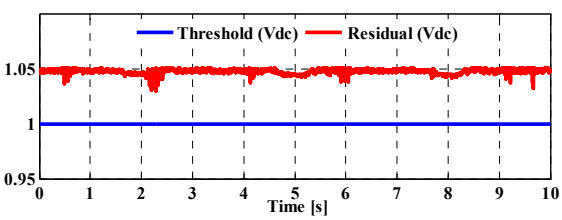

(k) Residual and threshold of DC-link voltage sensor fault.

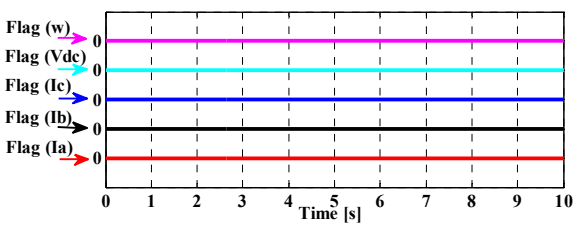

(l) Fault flags.

Fig. 8. Evolution of the proposed SMCSVO during speed reversal operations with healthy sensors.

redundancy with six sensors (two measurements of each phase current). A multiport switch is utilized to select the appropriate input, which is indicated by the control port in Fig. 5(a) (the first input indicates the state of the phase).

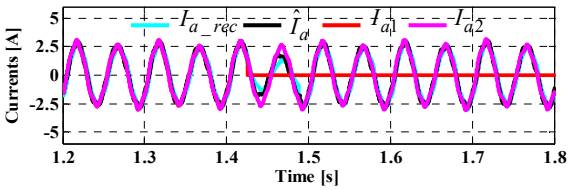

(a) Current sensors faults (a1 outage): measured phase "a" currents I_{a1} and I_{a2}, observed I_{a_obs}, and reconfigured I_{a_rec} currents.

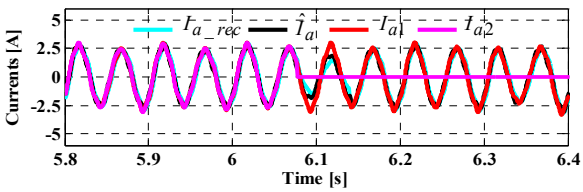

(b) Current sensors fault (a2 outage): measured phase "a" currents I_{a1} and I_{a2}, observed I_{a_obs}, and reconfigured I_{a_rec} currents.

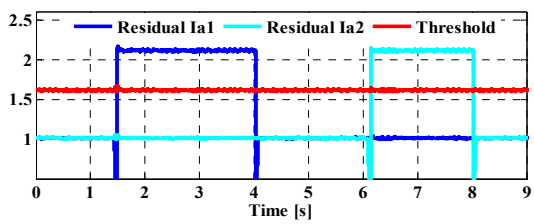

(c) Residual generation and thresholds of current sensors fault.

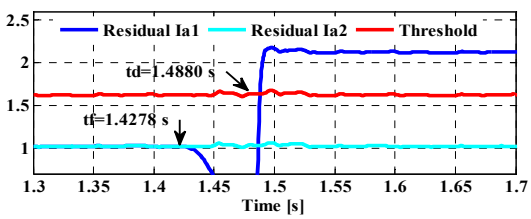

(d) Zoom: Residual generation and threshold of current sensor (a1) fault of phase (a).

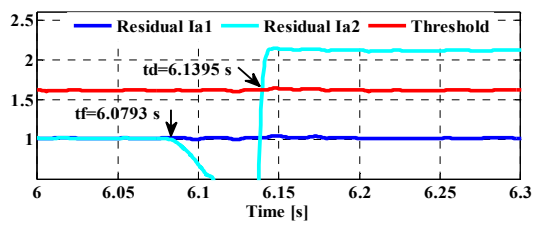

(e) Zoom: Residual generation and threshold of current sensor (a2) fault of phase (a).

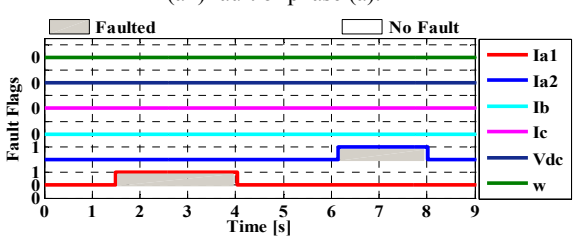

(f) Fault flags.

Fig. 9. Detection, localization, and reconfiguration of phase "a" current sensor faults (faults occur at time: sensor (a1) tf=1.4278 s and sensor (a2) tf=6.0793).

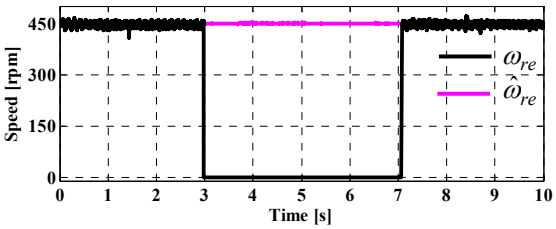

(a) Measured and observed rotor speeds.

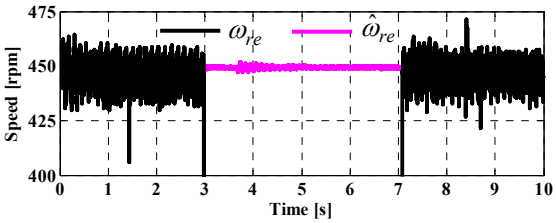

(b) Zoom of the measured and observed rotor speeds.

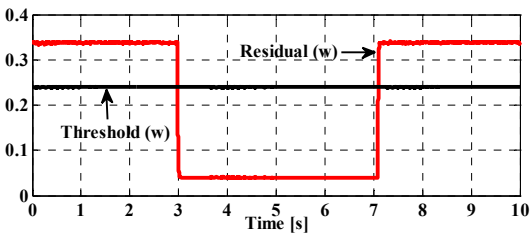

(c) Residual and threshold of speed sensor fault.

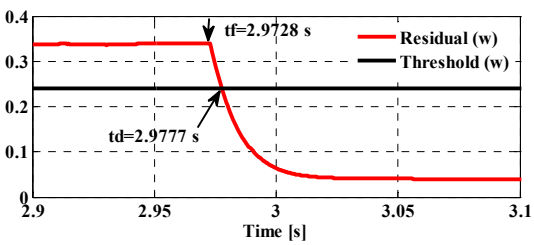

(d) Zoom of the residual and threshold.

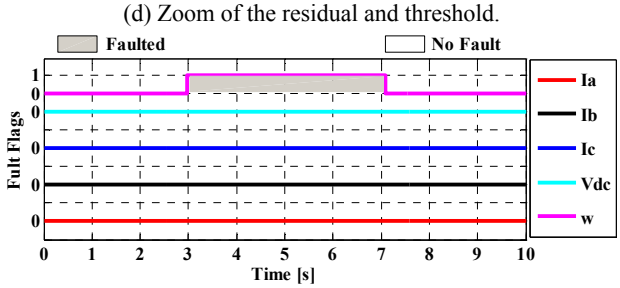

(e) Fault flags.

Fig. 10. Detection, localization, and reconfiguration of speed sensor fault.

In normal operations, the mean value of measurements is utilized as the input of the control loop and in the SMCSVO block.

In Fig. 9(a), the fault occurs at time tf=1.4278s (outage of sensor a1). The controller detects and isolates the fault and reconfigures from the measured I_{a1} to the measured I_{a2}. The control is reconfigured at td=1.4880 s. During the transient phase (Δt_{11}=60.2 ms), the value of I_{a_rec} is used in the control loop and in the SMCSVO block.

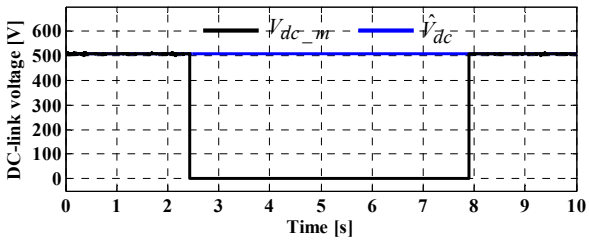

(a) Measured and observed DC-link voltage.

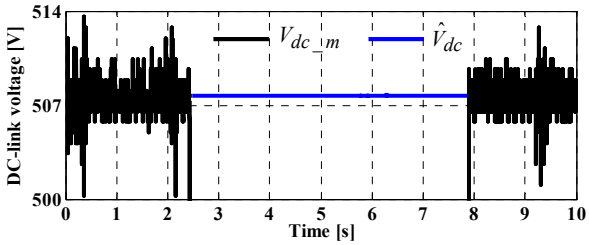

(b) Zoom of the measured and observed DC-link voltage.

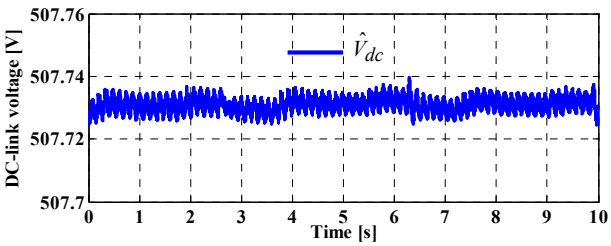

(c) Zoom of the observed DC-link voltage.

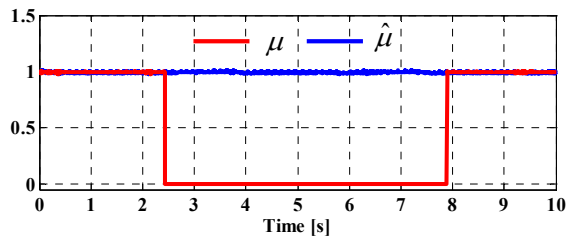

(d) Dynamic coefficients of DC-link voltage μ and $\hat{\mu}$.

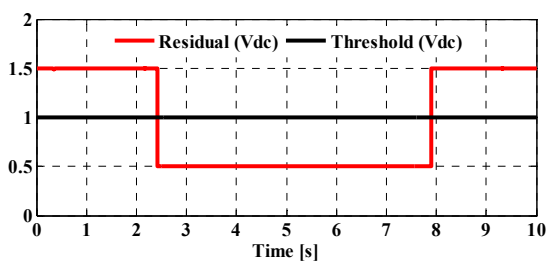

(e) Residual and threshold of DC-link voltage.

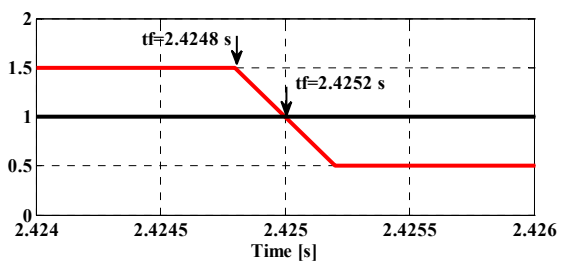

(f) Zoom: residual and threshold of DC-link voltage.

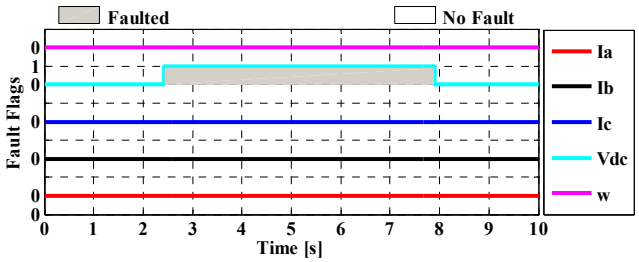

(g) Fault flags.

Fig. 11. Detection, localization, and reconfiguration of DC-link voltage sensor fault.

In Fig. 9(b), the next fault occurs at time tf=6.0793 s (outage of sensor a2). The controller detects and isolates the fault and reconfigures from the measured Ia2 to the measured Ia1. The control is reconfigured at td=6.1395 s. During the transient phase (ΔtI2=60.2 ms), the value of Ia_rec is used in the control loop and in the SMCSVO block. Practically, ΔtI1=ΔtI2.

The experimental results presented in Fig. 10 illustrate the diagnostic method's capability to diagnose speed sensor fault in the measurement chain. The operating conditions are as follows: ω_{re}=450rmp, T_L=15%Tn, V_{dc_n}=507.6V. The parameters of the FDLR algorithm are selected as ε=0.00005, $\xi_I=k_I$= 0.5, ξ_ω=0.04, ξ_{dc}=0.5.

The FDLR algorithm for speed sensor faults is presented in Section *3.2.2.B*. The scheme is based on software-measured and hardware-estimated speed. A multiport switch is used to select the appropriate input, which is indicated by the control port in Fig. 5 (the first input indicates the state of sensor speed).

In normal operations, the value of measured speed is utilized as the input of the control loop and in the SMCSVO block. When the sensor speed is in disagreement, the FDLR unit detects and isolates the speed sensor and reconfigures from the observed speed.

The experimental results presented in Fig. 11 illustrate the diagnostic method's capability to diagnose DC-link sensor fault "disconnection" in the measurement chain. The fault diagnostic performance is analyzed with sensor fault. A reference speed of 450 rpm has a load torque equal to 15% of the rated torque and a DC-link voltage equal to V_{dc_n}. The parameters of the FDLR algorithm are selected as ε=0.00005, $\xi_I=k_I$= 0.5, ξ_ω=0.04, ξ_{dc}=0.5.

In this test, the DC-link voltage sensor information is lost at tf=2.4248 s. Nevertheless, the DC-link voltage observer is maintained approximately equal to the rated DC-link voltage (507 V). The FDLR unit controller detects and isolates the fault and reconfigures from the measured DC-link voltage to the estimated one. The control is reconfigured at td=2.4252 s. During the transient phase (Δt_{dc}=0.4 ms), the value Vdc_rec is utilized to calculate the PWM signals.

V. Conclusion

In this study, fault detection, localization, and system reconfiguration of phase currents, speed/position, and DC-link voltage sensors in three-phase PMSM drives were presented. An SMO was utilized to estimate the stator currents, rotor speed/position, and DC-link voltage. The integration of adaptive threshold with SMO improves the safety and reliability of the PMSM drive system. The stability conditions of the SMO were verified through Lyapunov stability analysis.

The feasibility and effectiveness of the sensor fault diagnosis method were also analyzed through real-time experimental tests (from a prototype developed in the laboratory).

Appendix A

TABLE II
Specifications of the Test PMSM

	Parameters	Units	Values
Nameplate data of a PMSM	Rated voltage V_n	V	360
	Rated current I_n	A	5.9
	Rated power P_n	kW	3
	Rated frequency f_n	Hz	100
	Base speed ω_n	rpm	1500
	Rated torque T_n	N.m	19
Parameters determined by tests	Rated of pole pairs N_p	/	4
	Armature resistance R_s	Ω	2.144
	d-axis inductance L_d	mH	27.1
	q-axis inductance L_q	mH	28.8
	Magnet flux Linkage ψ_{pm}	Wb	0.2960
	Inertia moment J	kg.m^2	0.0032
	Friction coefficient B	Nm.s/rad	0.0008

TABLE III
Specifications of the PWM VSI
(from Semikron Datasheet)

Parameters	Units	Values
DC-link voltage (V_{dc} max)	V	750
Alternative voltage (V_{ac} max)	V	1200
Current line max (I_l max)	A	30
Rated power	kW	10
Switching frequency	kHz	15
Saturation voltage	V	2.2
Threshold voltage (IGBT)	V	1.7
Power supply (drives)	V	0/+15
Filtrage condensateurs (2 series)	2200 µF/400 V	
Dead time	µsec	4
Switching device	IGBT	
SEMIDRIVER	SKHI 22	

APPENDIX B

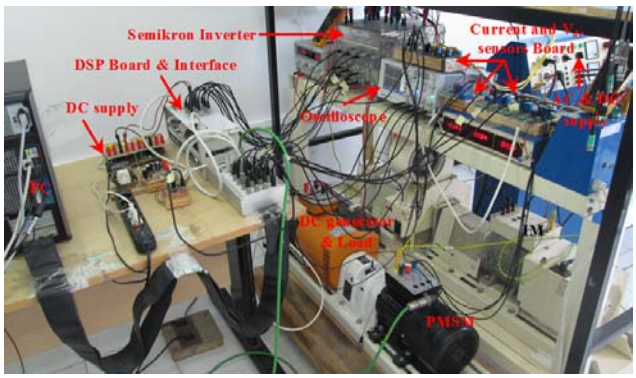

Fig. 12. Experimental platform in our laboratory (LAA/FHC /University of Boumerdes Algeria).

REFERENCES

[1] F. F. M. El-Sousy, "Robust wavelet-neural-network sliding-mode control system for permanent magnet synchronous motor drives," *IET Electric Power Applications*, Vol. 5, No. 1, pp. 113-132, Jan. 2011.

[2] S. K. Kommuri, J. J. Rath, K.C. Veluvolu, and M. Defoort, "Robust fault-tolerant cruise control of electric vehicles based on second-order sliding mode observer," in *14th International Conference on Control, Automation and Systems (lCCAS)*, pp. 698-703, Oct. 2014.

[3] S. C. Kim, T. H. Nguyen, D. C. Lee, K. B. Lee, and J. M. Kim, "Fault tolerant control of DC-link voltage sensor for three-phase AC/DC/AC PWM converters," *Journal of Power Electronics*, Vol. 14, No. 4, pp. 695-703, Jul. 2014.

[4] M. Aktaş, "A novel method for inverter faults detection and diagnosis in PMSM drives of HEVs based on discrete wavelet transform, " *Advances in Electrical and Computer Engineering*, Vol. 12, No. 4, pp. 33-38, 2012.

[5] C. Olivieri and M. Tursini, "A novel PLL scheme for a sensorless PMSM drive overcoming common speed reversal problems," in *IEEE International Symposium on Power Electronics, Electrical Drives, Automation and Motion(SPEEDAM)*, pp. 1051-1056, Jun. 2012.

[6] F. Meinguet, E. Semail, X. Kestelyn, Y. Mollet, and J. Gyselinck, "Change-detection algorithm for short-circuit fault detection in closed-loop AC drives," *IET Electric Power Applications*, Vol. 8, No. 5, pp. 165–177, May 2014.

[7] P. Pillay and R. Krishnan, "Modeling, simulation, and analysis of permanent-magnet motor drives, part I: the permanent-magnet synchronous motor drive," *IEEE Trans. Ind. Appl.*, Vol. 25, No. 2, pp. 265-273, Mar./Apr. 1989.

[8] W. S. Im, J. S. Kim, J. M. Kim, D. C. Lee, and K. B. Lee, "Diagnosis methods for IGBT open switch fault applied to 3-phase AC/DC PWM converter," *Journal of Power Electronics*, Vol. 12, No. 1, pp. 120-127, Jan. 2012.

[9] I. Jlassi, J. O. Estima, S. K. El Khil, N. M. Bellaaj, and A. J. M. Cardoso, "Multiple open-circuit faults diagnosis in back-to-back converters of PMSG drives for wind turbine systems," *IEEE Trans. Power Electron.*, Vol. 30, No. 5, pp. 2689–2702, May 2015.

[10] X. Zhang, G. Foo, M. D. Vilathgamuwa, K. J. Tseng, B. S. Bhangu, and C. Gajanayake, "Sensor fault detection, isolation and system reconfiguration based on extended Kalman filter for induction motor drives," *IET Electricic Power Applications*, Vol. 7, No. 7, pp. 607-617, Aug. 2013.

[11] Y. Yu, Z. Wang, D. Xu, T. Zhou, and R. Xu, "Speed and current sensor fault detection and isolation based on adaptive observers for IM drives," *Journal of Power Electronics*, Vol. 14, No. 5, pp. 967-979, Sep. 2014.

[12] G. H. B. Foo, X. Zhang, and D. M. Vilathgamuwa, "Sensor fault-resilient control of interior permanent-magnet synchronous motor drives," *IEEE/ASME Trans. Mechatronics*, Vol. 20, No. 2, pp. 855-864, Apr. 2015.

[13] Y. S. Jeong, S. K. Sul, S. E. Schulz, and N. R. Patel, "Fault detection and fault-tolerant control of interior permanent-magnet motor drive system for electric vehicle," *IEEE Trans. Ind. Appl.*, Vol. 41, No. 1, pp. 46-51, Jan./Feb. 2005.

[14] H. Lu, X. Cheng, W. Qu, S. Sheng, Y. Li, and Z. Wang, "A three-phase current reconstruction technique using single DC current sensor based on TSPWM," *IEEE Trans. Power Electron.*, Vol. 29, No. 3, pp. 1542-1550, Mar. 2014.

[15] T. Bernardes, V. F. Montagner, H. A. Gründling, and H. Pinheiro, "Discrete-time sliding mode observer for sensorless vector control of permanent magnet synchronous machine," *IEEE Trans. Ind. Electron.*, Vol. 61, No. 4, pp. 1679-169, Apr. 2014.

[16] H. Kim, J. Son, and J. Lee, "A high-speed sliding-mode observer for the sensorless speed control of a PMSM," *IEEE Trans. Ind. Electron.*, Vol. 58, No. 9, pp. 4069-4077, Sep. 2011.

[17] C. Chakraborty and V. Verma, "Speed and current sensor fault detection and isolation technique for induction motor drive using axes transformation," *IEEE Trans. Ind. Electron.*, Vol. 62, No. 3, pp.1943-1954, Mar. 2015.

[18] C. Choi, K. Lee, and W. Lee, "Observer-based phase-shift fault detection using adaptive threshold for rotor position sensor of permanent-magnet synchronous machine drives in electromechanical brake," *IEEE Trans. Ind. Electron.*, Vol. 62, No. 3, pp. 1964-1974, Mar. 2015.

[19] Z. Wang, L. Chang, and M. Mao, "Dc voltage sensorless control method for three-phase grid-connected inverters," *IET Power Electronics*, Vol. 3, No. 4, pp. 552–558, Jul. 2010.

[20] Q. T. An, L. Sun, and L. Z. Sun, "Current residual vector-based open-switch fault diagnosis of inverters in PMSM drive systems," *IEEE Trans. Power Electron.*, Vol. 30, No. 5, pp. 2814-2827, May 2015.

[21] U. M. Choi, F. Blaabjerg, and K. B. Lee, "Study and handling methods of power IGBT module failures in power electronic converter systems," *IEEE Trans. Power Electron.*, Vol. 30, No. 5, pp. 2517-2533, May 2015.

Aibeche Abderrezak was born in Bouhatem-Mila Algiers, Algeria. He received his B.S. and M.S. degrees in electrical engineering from University M'Hamed Bougara of Boumerdes FHC-UMBB, Algeria, in 2001 and 2009, respectively. He has been with the Department of Maintenance, Electrical Engineering Option, University of Boumerdes FSI-UMBB, Algeria, since 2013. Currently, he is a researcher at the Laboratory of Applied Automation, University M'Hamed Bougara of Boumerdes. His research interests include power converters, sensorless control of AC drives, fault diagnosis, and fault tolerant of AC drives and renewable energy.

Kidouche Madjid was born in Bordj-Menaiel, Algeria. He received his Electrical Engineering, Master of Sciences, and Ph.D degrees all in control theory. He joined M'hamed Bougara University of Boumerdes, Algeria in 1990 where he is a Professor in the department of automation and electrification of industrial process. He is a research group head on "Control of complex dynamical systems" at Applied Automatic Control Laboratory. He has been actively involved in several research projects in the fields of control and power system analysis. He is the author and co-author of numerous research publications in international conferences and journals. His research interests include modeling and control of dynamic non linear systems, stability of large scale systems, fuzzy and sliding mode control.